PHYSICS

Direct measurement of a non-Hermitian topological invariant in a hybrid light-matter system

Rui Su[1]*†, Eliezer Estrecho[2]*†, Dąbrówka Biegańska[2,3], Yuqing Huang[1], Matthias Wurdack[2], Maciej Pieczarka[2,3], Andrew G. Truscott[4], Timothy C. H. Liew[1,5], Elena A. Ostrovskaya[2]*, Qihua Xiong[6,7,8]*

Topology is central to understanding and engineering materials that display robust physical phenomena immune to imperfections. Different topological phases of matter are characterized by topological invariants. In energy-conserving (Hermitian) systems, these invariants are determined by the winding of eigenstates in momentum space. In non-Hermitian systems, a topological invariant is predicted to emerge from the winding of the complex eigenenergies. Here, we directly measure the non-Hermitian topological invariant arising from exceptional points in the momentum-resolved spectrum of exciton polaritons. These are hybrid light-matter quasiparticles formed by photons strongly coupled to electron-hole pairs (excitons) in a halide perovskite semiconductor at room temperature. We experimentally map out both the real (energy) and imaginary (linewidth) parts of the spectrum near the exceptional points and extract the novel topological invariant—fractional spectral winding. Our work represents an essential step toward realization of non-Hermitian topological phases in a condensed matter system.

INTRODUCTION

The discovery of topologically protected energy bands and associated topological phases in electronic materials has led to demonstrations of unique phenomena, such as dissipationless current (*1*) and enhanced sensitivity to electromagnetic fields (*2*, *3*), that have the potential to revolutionize the electronics industry. Inspired by the discoveries in the field of condensed matter physics, the realization of topological effects in engineered photonic systems holds similar promise for photonic applications (*4*). On the other hand, growing understanding of the physics of non-Hermitian systems with gain and loss (*5*, *6*) has led to demonstration of novel functionalities, such as loss-induced lasing (*7*), enhanced sensing (*8*, *9*), and optical nonreciprocity (*10*, *11*). The past few years have witnessed the convergence of the two research directions, with notable theoretical and experimental advances in extending the notion of topology to non-Hermitian systems (*12*, *13*). The bulk-boundary correspondence, the principle relating the surface states to the topological classification of the bulk, was generalized to non-Hermitian systems (*14*–*17*) and has been explored for high-order systems (*18*, *19*). Furthermore, the associated non-Hermitian skin effect, the localization of bulk modes at the edges of an open boundary system, was observed in experiments (*20*–*22*). A unique non-Hermitian topology arising from the winding of the complex eigenvalues (eigenenergies) was theoretically predicted (*23*–*25*). This is in stark contrast to energy-conserving systems, where the topological invariants are determined by the winding of the phase of the eigenstates in momentum space, which has been directly measured in ultracold atomic (*26*, *27*), microwave (*28*), and photonic systems (*29*). The properties of the eigenstates stemming from the novel non-Hermitian topology, such as the polarization half-charge (*30*) and localization of modes (*31*), have been experimentally observed in photonic and mechanical systems. However, a direct measurement of the non-Hermitian topological invariant in momentum space is yet to be demonstrated, regardless of the physical nature of the system under investigation.

Exciton polaritons, hybrid light-matter particles arising from strong coupling of confined photons to excitons in a semiconductor, offer a promising platform for investigations of topology and non-Hermitian physics in condensed matter. Artificial lattice potentials (*32*–*34*) enable exciton polaritons to emulate topological quantum matter (*35*), although the topological gap only opens in very strong magnetic fields requiring a superconducting magnet and cryogenic temperatures. Under similar extreme conditions, exciton-polariton systems also enable a direct measurement of physical quantities directly related to topology, such as the quantum geometric tensor (*36*), including the nonzero Berry curvature (*36*–*38*). Moreover, because of the photonic and excitonic losses, exciton polaritons are inherently non-Hermitian. A non-Hermitian spectral degeneracy—an exceptional point (EP) (*7*, *39*), where both the eigenvalues and eigenvectors coalesce—was demonstrated in exciton-polariton systems (*40*, *41*) in parameter space. Since then, new proposals have emerged combining topology and non-Hermiticity of the system using artificial lattices (*42*–*44*). However, there are no experimental studies yet demonstrating the novel topology arising from non-Hermiticity in exciton-polariton systems.

In this work, we exploit exciton polaritons formed in optically anisotropic lead-halide perovskite crystals embedded in an optical microcavity to demonstrate the emergence of non-Hermitian topology in an exciton-polariton system at room temperature. First,

[1]Division of Physics and Applied Physics, School of Physical and Mathematical Sciences, Nanyang Technological University, Singapore 637371, Singapore. [2]ARC Centre of Excellence in Future Low-Energy Electronics Technologies and Nonlinear Physics Centre, Research School of Physics, The Australian National University, Canberra 2601, Australia. [3]Department of Experimental Physics, Faculty of Fundamental Problems of Technology, Wrocław University of Science and Technology, Wyb. Wyspiańskiego 27, 50-370 Wrocław, Poland. [4]Laser Physics Centre, Research School of Physics, The Australian National University, Canberra 2601, Australia. [5]MajuLab, International Joint Research Unit UMI 3654, CNRS, Université Côte d'Azur, Sorbonne Université, National University of Singapore, Nanyang Technological University, Singapore, Singapore. [6]State Key Laboratory of Low-Dimensional Quantum Physics and Department of Physics, Tsinghua University, Beijing 100084, P.R. China. [7]Beijing Academy of Quantum Information Sciences, Beijing 100193, P.R. China. [8]Beijing Innovation Center for Future Chips, Tsinghua University, Beijing 100084, P.R. China.
*Corresponding author. Email: qihua_xiong@tsinghua.edu.cn (Q.X.); elena.ostrovskaya@anu.edu.au (E.A.O.); surui@ntu.edu.sg (R.S.); eliezer.estrecho@anu.edu.au (E.E.)
†These authors contributed equally to this work.

we develop a non-Hermitian model for the two states of exciton-polariton pseudospin that accounts for the inherent losses in the system. The exciton-polariton pseudospin originates from the two allowed projections of its spin on the structure axis and is directly related to the polarization of the exciton-polariton emission, i.e., cavity photoluminescence (PL) (*45*). The model predicts the formation of two paired EPs in momentum space connected by the topologically protected bulk Fermi arcs (*30*). We also demonstrate theoretically that the topologies of the eigenstates (polarization winding) and the eigenenergies (spectral winding) are not equivalent, and the latter can persist when the former is absent. Then, by performing spectroscopic measurements of exciton-polariton PL, we experimentally confirm the existence of paired EPs and Fermi arcs linking them in momentum-resolved spectrum. Moreover, the non-Hermiticity results in the appearance of circular polarization, maximized near the EPs (*46*), which arises from the imaginary part of the artificial in-plane magnetic field acting on the exciton-polariton pseudospin. We provide a direct measurement of the novel non-Hermitian topological invariant—spectral winding—in a spatially homogeneous system and demonstrate the topological stability of the EPs and Fermi arcs against the gap-opening perturbations.

RESULTS

Non-Hermitian model for exciton-polariton dispersion

Losses are unavoidable in exciton-polariton systems because of the finite lifetimes of the cavity photons and excitons. These losses can be fully accounted for using non-Hermitian framework, where both exciton and photon resonances in the cavity are described by complex energies $\widetilde{E} = E - i\gamma$, with the real part corresponding to the resonance energy and the imaginary part to the linewidth (inverse lifetime). We therefore model the complex exciton-polariton dispersion (spectrum in momentum space) by using a 4 × 4 non-Hermitian Hamiltonian describing the coupling of the two polarization modes of the cavity photons to the corresponding modes of the exciton (*47*)

$$H(\boldsymbol{k}) = \begin{pmatrix} H_c(\boldsymbol{k}) & V\mathbf{1}_{2\times2} \\ V\mathbf{1}_{2\times2} & \widetilde{E}_x\mathbf{1}_{2\times2} \end{pmatrix} \quad (1)$$

where $\hbar\boldsymbol{k}$ is the in-plane momentum, $\mathbf{1}_{2\times2}$ is the 2 × 2 identity matrix, $\widetilde{E}_x = E_x - i\gamma_x$ is the complex exciton energy, and V is the exciton-photon coupling strength. For simplicity, we assume that the exciton spins are degenerate in energy, and the coupling strength is isotropic. We model the cavity photon by extending the Hermitian Hamiltonian (*48*, *49*) to properly account for the losses

$$H_c(\boldsymbol{k}) = \begin{pmatrix} \widetilde{E}_c(k) & \widetilde{\alpha} + \widetilde{\beta}(k)\, e^{-2i\phi} \\ \widetilde{\alpha} + \widetilde{\beta}(k)\, e^{2i\phi} & \widetilde{E}_c(k) \end{pmatrix} \quad (2)$$

where ϕ is the in-plane propagation angle, $\widetilde{E}_c(k) = \widetilde{E}_{c0} + \widetilde{\chi}(k)$ is the mean complex energy of the cavity photon, $\widetilde{\chi}(k)$ is a function related to the effective mass (real part) and the momentum-dependent loss rates (imaginary part), $\widetilde{\alpha}$ describes the complex energy splitting due to *X*-*Y* splitting, and $\widetilde{\beta}(k)$ describes transverse-electric transverse-magnetic (TE-TM) splitting. The *X*-*Y* splitting can arise from the birefringence in the cavity medium (*48*, *49*), for example, due to the anisotropic orthorhombic crystal structure of perovskites at room temperature (*33*, *50*), which leads to different cavity lengths for the ordinary and extraordinary waves and results in the splitting of both energies and linewidths at normal incidence ($k = 0$). The TE-TM splitting naturally arises from the polarization-dependent reflectivity of the dielectric mirrors at oblique angles, inducing an effective spin-orbit coupling (*48*–*50*) that increases with the angle of incidence (or k). The resulting energy splitting is sensitive to the position of the cavity resonance with respect to the distributed Bragg reflector (DBR) stopband, but the linewidth consistently increases (decreases) with momentum for TE (TM) modes (*47*). The model Eqs. 1 and 2 are derived by extracting the resonances in 4 × 4 transfer matrix simulations (*46*) (see Materials and Methods). The behavior of the energies and linewidths is presented in the Supplementary Materials.

In the strong coupling regime, the model Eqs. 1 and 2 result in four exciton-polariton branches (see the Supplementary Materials). In this work, we focus on the two lower polariton branches since the upper branches are not visible in PL experiments. The lower polaritons at lower momenta k can be described by a model similar to Eq. 2. However, the effective *X*-*Y* and TE-TM splitting parameters $\widetilde{\alpha}$ and $\widetilde{\beta}$ now also depend on the exciton-photon coupling strength V and exciton-photon detuning $\widetilde{E}_{c0} - \widetilde{E}_x$. In experiments, the exciton-photon coupling strength is typically fixed, but the exciton-photon detuning can be varied across the sample because of distinct cavity lengths. The effective 2 × 2 Hamiltonian can be recast into a more convenient form as $\widetilde{E} = \langle\widetilde{E}(\boldsymbol{k})\rangle 1_{2\times2} + \boldsymbol{G}(\boldsymbol{k}) \cdot \sigma$, where $\langle\widetilde{E}(\boldsymbol{k})\rangle$ is the mean lower polariton complex energy, $\sigma = [\sigma_x, \sigma_y, \sigma_z]^T$ is a vector of Pauli matrices, and

$$\boldsymbol{G}(\boldsymbol{k}) = [\widetilde{\alpha} + \widetilde{\beta}(k)\cos 2\phi, \widetilde{\beta}(k)\sin 2\phi, 0] \quad (3)$$

is the effective non-Hermitian gauge field. The complex spectrum can be written as $\widetilde{E}_{\pm} - \langle\widetilde{E}\rangle = \pm\sqrt{G_R^2 - G_I^2 + 2i\boldsymbol{G}_R \cdot \boldsymbol{G}_I}$, where G_R and G_I are the real and imaginary parts of the gauge field, respectively. In the Hermitian limit of negligible losses, the spectrum (energy eigenvalues) of the Hamiltonian with gauge field, Eq. 3, features two Dirac cones in momentum space, as shown by the energy surfaces in Fig. 1 (A and B). This lossless approximation has been successfully used to describe several experiments in exciton-polariton systems such as the optical spin-Hall effect (*45*), anomalous Hall effect (*36*), and the measurement of the quantum geometric tensor (*36*–*38*). Adding a real-valued σ_z component to the gauge field, Eq. 3, e.g., by inducing a Zeeman shift of the exciton energies with an out-of-plane magnetic field, would remove the Hermitian degeneracies at the Dirac point and thus open a topological gap (*36*–*38*). When polarization-dependent losses are non-negligible, the imaginary parts of the gauge field, Eq. 3, split each of the Dirac point into a pair of EPs, as shown in Fig. 1 (C and D). These EP pairs are topologically stable (*12*), in stark contrast to the Dirac points that are only stable when protected by symmetry. It takes a strong gap-opening perturbation (i.e., a real-valued σ_z term) to make the EPs approach each other (see Fig. 1E) and annihilate to open the gap (see Fig. 1F). A closer look at one of the pairs, as shown in Fig. 1 (C and D), reveals that the paired EPs are connected by open arcs called the bulk Fermi arc (*30*), where $\Delta E = 0$ (green), and the imaginary Fermi arc, where $\Delta\gamma = 0$ (orange), which form closed contours in momentum space (see Fig. 1G). The gap opens when the bulk Fermi arc shrinks and disappears, and the imaginary Fermi arc closes.

Non-Hermitian systems are characterized by two nonequivalent types of topological winding numbers: The first one is a topological

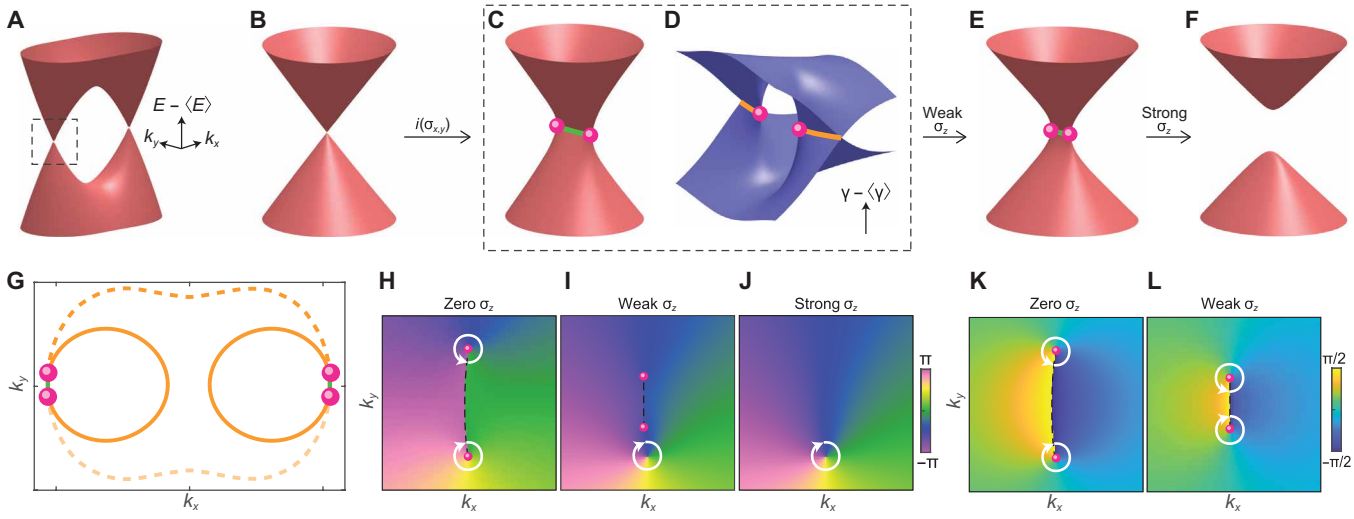

Fig. 1. Complex spectral structure near pairs of EPs in momentum space. (**A**) Energy (real part of the complex spectrum) of the exciton-polariton modes in a microcavity with linear birefringence, calculated using the model Eq. 1. The mean energy is subtracted for clarity. Energy crossings occur at two opposite regions in the 2D momentum space (k_x, k_y). (**B**) Enlarged view of the dashed region in (A) in the Hermitian limit, showing a Dirac point. (**C**) Energy of the dashed region in (A) in the non-Hermitian case, with nonzero $i\sigma_{x,y}$ components, showing the Dirac point splitting into a pair of EPs (pink dots) connected by the nodal line, bulk Fermi arc (green), where the energies cross. (**D**) Imaginary part of the complex spectrum corresponding to the linewidth for the dashed region in (A), showing the imaginary Fermi arc (orange), where the linewidths cross, emanating from the EPs (pink dots). (**E**) Energy of the system with a weak, real-valued σ_z term perturbation. (**F**) Same as (E) but with a strong perturbation leading to the annihilation of the EPs and opening of the gap. (**G**) Simplified complex energy structure of the two eigenstates, showing the bulk (green) and imaginary (orange) Fermi arcs connecting at the EPs and forming two closed contours. A single contour can also form (dashed orange) for the different sign of the parameters in Eq. 3. (**H** to **J**) In-plane pseudospin angle in momentum space of the upper eigenstate corresponding to (from left to right) (C), (E), and (F), respectively. (**K** and **L**) Spectral phase Arg($\Delta\tilde{E}$) in momentum space corresponding to (C) and (E), respectively. In (H) and (I), pink dots correspond to the EP, dashed lines correspond to the bulk Fermi arc, and white arrowed contours correspond to the half-charge (H, K, and L) and integer (I and J) windings around the singularities.

charge of the eigenstates (or pseudospin) arising around singularities in momentum space, and the second one is the non-Hermitian topological charge associated with eigenenergies. For the case of Eq. 3, there are pairs of singularities in the pseudospin texture, around which the in-plane pseudospin component winds. As shown in Fig. 1H for the upper eigenstate, the in-plane pseudospin angle rotates by ±π around the singularity due to the π discontinuity at the bulk Fermi arc, resulting in half-integer topological charges (*30*). The lower eigenstate exhibits the same topological charges at the same singularities (see the Supplementary Materials). Moreover, the pseudospin is polarized up or down at these points, which translates to circularly polarized PL emission (*51*), exactly at the momenta of the paired EPs (see the Supplementary Materials).

Adding a chiral (or σ_z) term to Eq. 3, which can be achieved by magnetically induced Zeeman splitting (*36*), or intrinsic chirality (optical activity) (*38*), moves the EPs in momentum space, but the pseudospin singularities remain at the same momenta, a phenomenon closely related to the haunting theorem in singular optics (*51*). The singularities reside in separate eigenstates, and the topological charge becomes integer-valued. These effects are demonstrated in Fig. 1I for a weak, real-valued σ_z perturbation, where one singularity disappears, since it migrates to the other eigenstate (see the Supplementary Materials), and the winding of the remaining one is −2π. The integer topological charges persist even if the gap opens. Moreover, with increasing magnitude of the σ_z term, the polarization at the EP becomes elliptical, and the discontinuity at the bulk Fermi arc continuously decreases toward zero where the gap opens, as shown in Fig. 1J (see also the Supplementary Materials). The half-integer winding, shared by the two eigenstates, is therefore unstable against any σ_z perturbation, where a nonzero σ_z term suddenly switches the winding from π to 2π (or to zero for the other eigenstate). This transition is reminiscent of the Hermitian case, where the σ_z perturbation immediately destroys the Dirac point and opens the gap.

In contrast to the topology of the eigenstates described above, the winding of the eigenenergies is deeply tied to the EP and is topologically stable. The topology is revealed by the "spectral phase" of the difference of the two complex energies Arg($\Delta\tilde{E}$) (*23*–*25*). As shown in Fig. 1 (K and L), the singularities of the spectral phase occur exactly at the EP with a π-spectral phase winding or half-integer topological charge, regardless of where the singularities of the eigenstates are located in momentum space. This is because the spectral phase jump at the bulk Fermi arc remains equal to π. These two features, the π-winding and the π-phase jump, persist even under a weak, real-valued σ_z perturbation, as shown in Fig. 1L. This is in contrast with the behavior of the eigenstates, where the π winding suddenly switches to 2π (Fig. 1, H and I), and the phase jump across the bulk Fermi arc decreases with a σ_z perturbation (see the Supplementary Materials).

At sufficiently strong σ_z perturbation, the EPs meet and annihilate, the gap fully opens, and the non-Hermitian topological charges disappear, but the topological charges of the eigenstates (polarization vortices) remain (see Fig. 1J). This demonstrates that the topologies of the eigenstates and the eigenenergies are separable, and measuring the topology of the eigenstates, in general, is not equivalent to measuring the non-Hermitian topology of the eigenenergies. In the following, we experimentally observe paired EPs in an exciton-polariton system with weak chirality and directly measure the non-Hermitian topological invariant by extracting the winding of complex eigenenergies from the PL spectrum.

Experimental observation of paired EPs

To demonstrate the EP pairs in the exciton-polariton dispersion experimentally, we use the microcavity schematically shown in Fig. 2A. It is formed by sandwiching a ~142-nm-thick $CsPbBr_3$ perovskite crystal between two SiO_2/Ta_2O_5 DBRs, as detailed in Materials and Methods. The crystal is optically anisotropic because of its orthorhombic symmetry (*33*, *52*, *53*), which leads to *X*-*Y* splitting of the exciton-polariton states (*33*, *50*). The exciton polaritons are excited by an off-resonant laser with the photon energy far above the perovskite exciton energy. The exciton-polariton energy distribution in momentum space is extracted from the PL of the sample. An emitted photon at polar angle θ, azimuthal angle ϕ (see schematics in Fig. 2B), and photon wavelength λ carries the exciton-polariton in-plane momentum $\hbar\boldsymbol{k} = \hbar\left(\frac{2\pi}{\lambda}\right)\sin\theta(\cos\phi, \sin\phi)$, with ϕ corresponding to the propagation angle. To distinguish between the pseudospin states of exciton polaritons, which translate to the polarization of the PL, the signal is recorded with linear polarizations along the horizontal-vertical (H-V) (orientation shown in Fig. 2B), diagonal-antidiagonal (D-A), and left-right circular polarizations (L-R). The sample is oriented so that the *X*-*Y* splitting, along with the spin-orbit coupling, results in energy crossing along (k_x, $k_y = 0$) but no crossing along ($k_x = 0$, k_y) in the linearly polarized exciton-polariton dispersions (*36*, *37*), as shown in Fig. 2C.

The non-Hermitian character of the exciton-polariton dispersion is reflected in the linewidths of the modes, which are also split at $k = 0$ (see fig. S2). Subtracting the mean value, i.e., $\gamma - \langle\gamma\rangle$, reveals that the linewidth dependence on k is also anisotropic as shown in Fig. 2D, such that the linewidth switches or crosses along the direction (k_x, $k_y = 0$) but not along ($k_x = 0$, k_y). The crossings in energy and linewidth along the same direction suggest that the Fermi arcs form two loops in momentum space, as shown by the insets of Fig. 2C. A similar behavior of energy and linewidth in momentum space was observed for the cavity photons in birefringent ZnO-based microcavities (*46*, *54*) in the weak coupling regime (i.e., without coupling to excitons). However, the paired EPs remained elusive in the strong coupling regime despite several experiments on exciton polaritons in anisotropic cavities (*36*–*38*, *55*). Related EPs in momentum space were observed in microcavities with embedded carbon nanotubes (*56*) and organic microcrystals (*57*), but strong exciton-photon coupling in these systems only occurs in one polarization. Our results demonstrate that the exciton polaritons can inherit the EPs from birefringent cavity photons.

The EPs predicted in Fig. 1 (C and D) are expected to exist near the energy crossings at $\boldsymbol{k}^* \approx (\pm 5.2, 0)\ \mu m^{-1}$ (see Fig. 2C). The position of the EP pair can be determined by carefully tracking the complex spectrum near this region. The extraction of peak energy and linewidth from the polarized PL measurements is detailed in Materials and Methods. Figure 3 shows the results of the measurements along five lines (labeled b to f) in *k*-space that intersect the Fermi arcs as schematically shown in Fig. 3A. The measurement in Fig. 3B is approximately along the bulk Fermi arc, where the mode energies approach each other while the linewidths clearly repel. At a slightly off-arc position, as shown in Fig. 3C, the mode energies always repel, but the linewidths cross at two points of the imaginary Fermi arc. Perpendicular to the bulk Fermi arc and close to the EP, the energies cross while the linewidths approach each other, as shown in Fig. 3D. Conversely, the modes cross in linewidth and approach in energy outside the bulk Fermi arc but close to the EP, as shown in Fig. 3F. Across the middle of the bulk Fermi arc, Fig. 3E clearly shows that the energies cross, but the linewidths repel. From these results (see fig. S5 for the 2D surfaces), we estimate the EP positions to be $\boldsymbol{k}_{EP} \approx (-5.2, 0.40)\ \mu m^{-1}$ and $\boldsymbol{k}_{EP} \approx (-5.2, 0.09)\ \mu m^{-1}$ with a bulk Fermi arc length of $\approx 0.31\ \mu m^{-1}$.

Pseudospin texture in the complex artificial gauge field

The existence of the EPs is further evidenced by the circular polarization of the exciton-polariton emission (*9*, *46*), which corresponds to the singularities of the eigenstates near the EPs (see Fig. 1, H and I) where the exciton-polariton pseudospin points either up or down. We define the pseudospin of the eigenstates using the Stokes parameters:

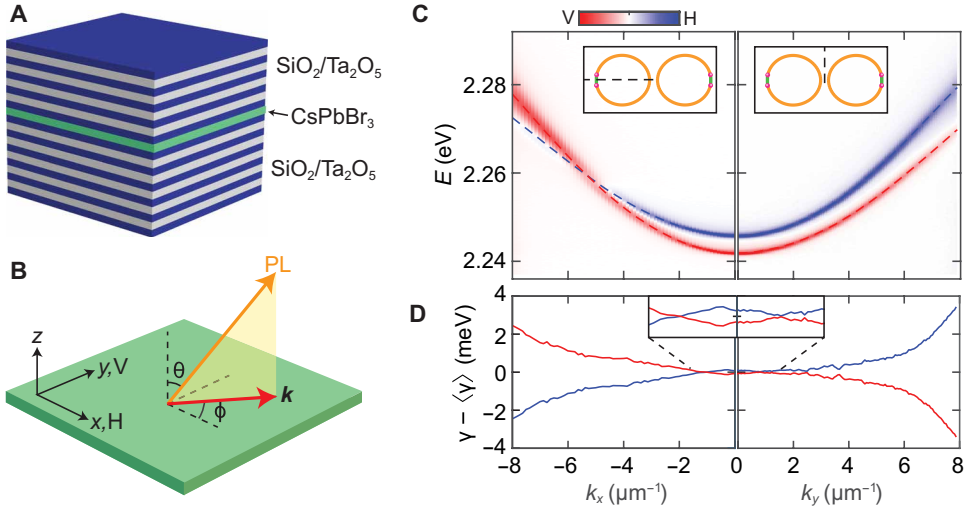

Fig. 2. Experimental investigation of the complex exciton-polariton eigenenergies. (**A**) Schematics of the planar microcavity made of SiO_2/Ta_2O_5 DBRs with an embedded $CsPbBr_3$ perovskite crystal. (**B**) Schematics of the laboratory (*x*, *y*, *z*) axis and the polarization measurement axis (H, V). The exciton-polariton in-plane momentum depends on the angles (θ,ϕ) of the PL emission. (**C**) Linearly polarized PL intensity (I_V-I_H) measured along (k_x, $k_y = 0$) and ($k_x = 0$, k_y). Dashed lines are the extracted peak energies of the two polarized modes. The dispersion is approximately symmetric for $k \rightarrow -k$. Inset: Schematics of the measurements in momentum space with respect to the Fermi arcs. (**D**) Linewidths of the modes in (C) with the mean subtracted. Inset: Enlarged region near $k = 0$.

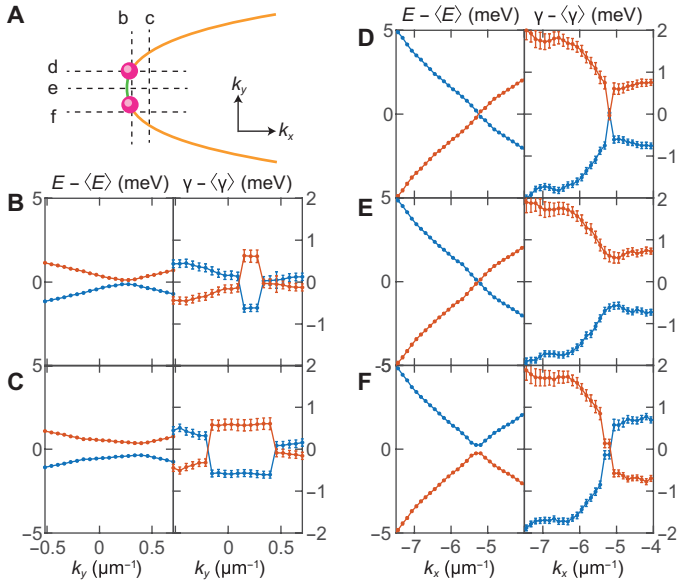

Fig. 3. Mapping out complex energies near the EP pair. (**A**) Schematics of the EP pair (pink dots) connected by the bulk (green) and imaginary (orange) Fermi arcs. Dashed lines (b to f) represent the lines (directions) in *k*-space, along which the measurements in (B) to (F) are performed. (**B** to **F**) Measured energies and linewidths (mean-subtracted) of the two modes: (B) Parallel to and very near the bulk Fermi arc; (C) parallel to the bulk Fermi arc intersecting the imaginary Fermi arc twice, which corresponds to two linewidth crossings and no crossing in energy; (D) perpendicular to the bulk Fermi arc very near the top EP, showing crossing in both energy and linewidth; (E) along the center of the real Fermi arc, showing crossing in energy and anticrossing in linewidth; (F) near the EP but outside the real Fermi arc showing no crossing in energy but crossing in linewidth. The complex eigenvalues are sorted so that a smooth crossing (D and E) or anticrossing (B, C, and F) in the real part is ensured. The values for *k* are as follows: (B) $k_x = -5.19$ μm^{-1}, (C) $k_x = -5.07$ μm^{-1}, (D) $k_y = 0.40$ μm^{-1}, (E) $k_y = 0.21$ μm^{-1}, and (F) $k_y = 0.09$ μm^{-1}. Error bars represent the 95% confidence interval fitting results.

$S_1 = (I_H - I_V)/(I_H + I_V)$, $S_2 = (I_D - I_A)/(I_D + I_A)$, and $S_3 = (I_R - I_L)/(I_R + I_L)$. In the Hermitian limit, and since Eq. 3 does not have a σ_z term, the eigenstates are orthogonal and purely linearly polarized (*48*), with the corresponding pseudospins confined to the S_1-S_2 plane of the Poincaré sphere (orthogonal polarizations are antipodal), as shown by the thin red and blue arrows in Fig. 4A. However, due to non-Hermiticity, the eigenstates of the Hamiltonian are not orthogonal, and the pseudospins of the eigenstates tend to point in the same direction toward one of the poles, as shown by the thick red and blue arrows in Fig. 4A. This leads to a nonzero S_3 Stokes component, while the projections on the S_1-S_2 plane remain antipodal. Hence, both eigenstates have the same S_3 components (dashed arrows in Fig. 4A), which, in this case, is a measure of the non-Hermiticity of the Hamiltonian. At the EP, full alignment occurs, resulting in a merged eigenstate pointing to the pole with a purely circular polarization, as shown by the purple arrow in Fig. 4A. The calculated circular polarization or S_3 component of the pseudospin texture of either eigenstate in *k*-space is shown in Fig. 4B. Maximum circular polarization occurs at the EPs and gradually decreases away from them. The EPs within the pair have opposite chirality, and the two pairs have opposite orientations.

The appearance of chirality in the model arises from the interplay between the real and imaginary components of the purely in-plane complex artificial magnetic field. If the real and imaginary fields are parallel or purely real or imaginary, the pseudospin of the eigenstates tends to align (parallel or antiparallel) to the field. However, if the two fields have perpendicular components, the pseudospins tend to align away from the real and imaginary parts and toward each other, which, in our case, effectively induces an out-of-plane component. The effective out-of-plane component is different from a real-valued out-of-plane magnetic field, where the pseudospins of the two modes remain antipodal on the Poincaré sphere. This non-Hermitian generalization allows an arbitrary control of the polarization (*58*) and can lead to rich spin dynamics not achievable with real-valued artificial magnetic fields. Note that in this off-resonant (incoherent) regime of exciton-polariton excitation, we are measuring the pseudospin of the eigenstates. This is in contrast to the resonant (coherent) regime, where a nonzero S_3 component can result from pseudospin precession in an in-plane field (*45*).

We take advantage of the non-Hermiticity, which results in nonorthogonal and chiral eigenstates, to directly measure the S_3 or spin texture of the exciton polaritons, as shown in Fig. 4C, by capturing the momentum space distribution without resolving the two modes. This method assumes that the two eigenstates at a momentum $\boldsymbol{k}$ are equally occupied, which is not always the case. However, it is effective for finding the pseudospin singularities shown in Fig. 1(H and I). A circular polarization texture qualitatively similar to the prediction of the model is observed using this method, with the local extrema near the EPs (black points in Fig. 4C). The discrepancy between the momenta of the EPs and the extrema of the S_3 texture is due to the close proximity of the EPs. The opposite circular polarization in the vicinity of the paired EPs tends to overlap and cancel each other. Hence, the measured $|S_3|$ is greatly reduced, and the extrema are offset away from the EPs (see the Supplementary Materials for supporting simulations). A similar low level of circular polarization degree near the EPs was observed for microcavity photons without coupling to excitons (*54*).

In addition to the spin texture due to the EPs, there is a background circular polarization (or chirality) that is not accounted for in the model Eqs. 1 and 2. This originates from the exciton emission of the bare perovskite (see the Supplementary Materials). The observed chirality can arise from the chirality of the excitons in lead-halide perovskites (*59*, *60*), but further experimental work is needed to verify its origin and derive an effective model for its spin texture. Here, we treat the chirality as a weak σ_z perturbation to Eq. 3, which can move the EPs toward each other and potentially open the gap in the Hermitian limit (see Fig. 1) (*38*). The clear observation of EPs in our experiment therefore demonstrates the topological stability of EP pairs against gap-opening (chiral) perturbations or any perturbation in general (*12*). The weak chirality places the experiment in the regime shown in Fig. 1(E, I, and L), where the topologies of the eigenstates and eigenenergies are not related to each other.

Observation of non-Hermitian topological invariant

Last, with the existence of the EPs verified using both the complex energies and pseudospin texture, we demonstrate the direct measurement of the non-Hermitian topological invariant arising from the EPs in momentum space. For the two-level system considered here, the non-Hermitian topological invariant, called the "spectral winding" or "vorticity" (*23*–*25*), is formally defined as

$$w = -\frac{1}{2\pi}\oint_C \nabla_{\boldsymbol{k}} \arg\left[\tilde{E}_+(\boldsymbol{k}) - \tilde{E}_-(\boldsymbol{k})\right] \cdot d\boldsymbol{k} \quad (4)$$

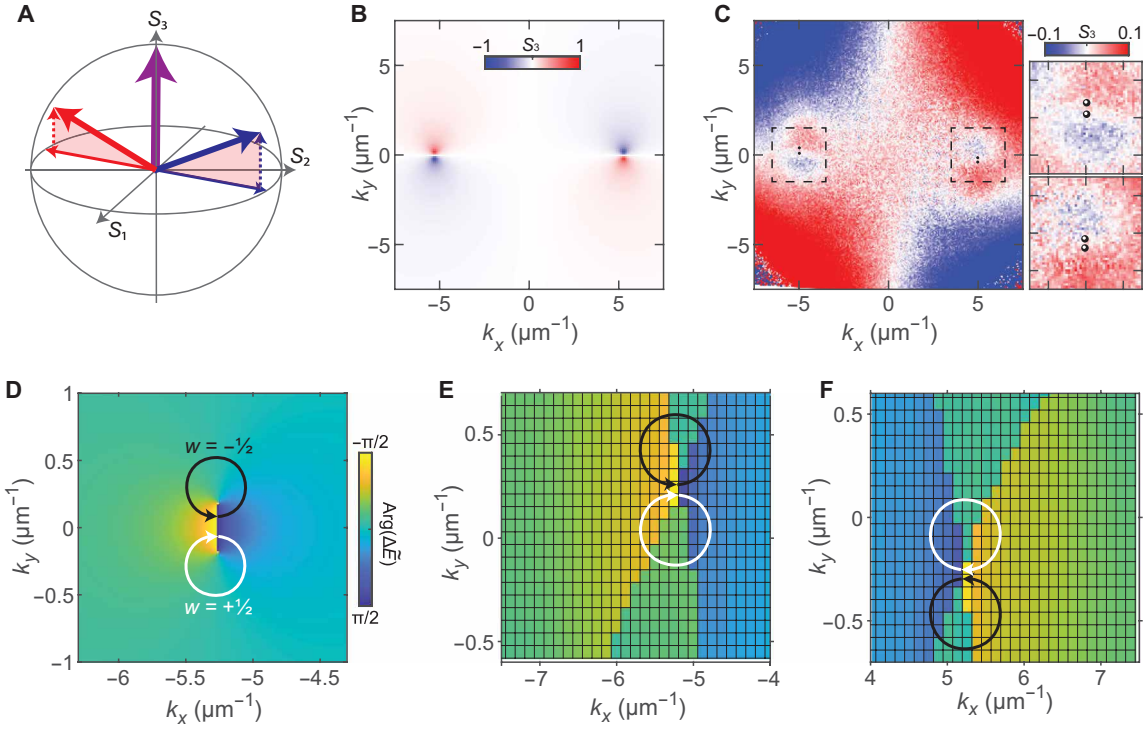

Fig. 4. Chirality and topology of the EPs. (**A**) Poincaré sphere with arrows representing the pseudospin of exciton polaritons away from the EP (thin red and blue), near the EP (thick red and blue), and at the EP (thick purple). Dashed vertical arrows are the effective out-of-plane field arising from the imaginary component of the complex in-plane artificial magnetic field. (**B**) Theoretical texture of circular polarization (S_3) arising from the inclusion of non-Hermiticity into the model of Eq. 1. (**C**) Measured energy-integrated circular polarization (S_3) showing the same spin structure as in (B) but with a weak S_3 background coming from the bare perovskite (see section: Pseudospin texture in the complex artificial gauge field). Right: Enlarged images of the marked regions showing the position of EPs (black points). (**D**) Theoretical values of arg($\tilde{E}_+ - \tilde{E}_-$) for one EP pair with the arrows schematically showing the fractional winding number. Parameters are the same as in Fig. 1 (C and D). (**E** and **F**) Measured values of arg($\tilde{E}_+ - \tilde{E}_-$) near the two pairs of EPs demonstrating the half-integer spectral winding around each EP.

where C is a closed loop in k-space. Naturally, this topological invariant is zero for Hermitian systems. The topology depends on the scalar field $\arg[\tilde{E}_+(\boldsymbol{k}) - \tilde{E}_-(\boldsymbol{k})]$, a spectral phase that is well defined everywhere except at the EPs. Hence, the EPs are sources of non-Hermitian topological charges. For the paired EPs considered here, the theoretical spectral phase calculated from model Eq. 3 rotates in opposite directions around each EP, forming oppositely charged spectral vortices, as shown in Fig. 4D. The spectral vortices have a half-integer charge (*23*) since the spectral phase acquired around the loop enclosing a single EP is $\pm\pi$.

By carefully measuring the energies and linewidths in the vicinity of the EP pairs, we are able to extract the spectral phase and consequently determine the winding of the complex eigenenergies, as presented in Fig. 4 (E and F). The spectral phase winds around the EPs and jumps by approximately π at the bulk Fermi arc that connects the EPs. The small phase jumps away from the EP pair are experimental artifacts where we switch between H-V and D-A polarized measurements (see Materials and Methods) to extract the energies and linewidths. Using the definition in Eq. 4, we can assign a ±1/2 non-Hermitian topological charge to the EPs, as annotated in Fig. 4D and symbolized by the black and white arrows in Fig. 4 (E and F). Each pair of EPs therefore forms a "topological dipole," and the two dipoles have opposite orientations, as predicted by the model in Fig. 4B. Furthermore, the spectral winding around the whole EP pair is zero. Consequently, if the separation of the EP pair is not resolved in the experiment, the non-Hermitian topological invariant would not be measurable.

It is important to stress that the topological winding of the eigenenergies measured here should, in principle, be accompanied by the half-integer winding of polarization (*30*), as theoretically demonstrated in Fig. 1 (H and K). However, because of the background S_3, which introduces a weak σ_z term perturbation, the measured spectral winding is no longer related to the winding of the polarization (see Fig. 1, I and L). Hence, the non-Hermitian topological invariant observed in this work is fundamentally different from the winding of the eigenstates observed in photonic systems (*30*). Moreover, the measured half-integer topological invariant is unaffected by the chirality observed in the experiment, as theoretically demonstrated in Fig. 1L. This is not the case for the polarization winding that would become integer-valued even for weak chiral perturbation.

DISCUSSION

In summary, we have demonstrated the existence of paired EPs in the momentum-resolved exciton-polariton spectrum and directly measured the non-Hermitian topological invariant arising from the half-integer winding of the exciton-polariton complex eigenenergies around the EPs. We have also shown theoretically that the topology of the eigenstates and eigenenergies is separable, and hence, the signatures of inherent topology of EPs previously observed in the eigenstates of classical wave systems (*30*, *31*) are fundamentally different from our observation.

In contrast to previously demonstrated EPs in parameter space of exciton-polariton systems (*40*, *41*, *56*), the EPs in momentum

space observed here are expected to have a direct influence on the system's dynamics (*61*). Our observation can potentially lead to the realization of non-Hermitian topological phases (*24*) and the predicted nontrivial dynamics, such as a non-Hermitian skin effect (*62*), without the need for sophisticated microstructuring of the sample (*43*) or strong external magnetic fields (*35*). Moreover, we have demonstrated the manifestation of the imaginary part of the artificial gauge field that tends to align the exciton-polariton pseudospin pair toward each other and perpendicular to the field direction. This may lead to a new type of spin precession (*58*) and dynamics of exciton polaritons that is not possible in real magnetic fields. Combined with advanced methods for potential landscaping (*32*) and the possibility to extract a wide range of observables from the cavity PL, our work affirms exciton polaritons as a solid-state platform for exploring robust topological phenomena that do not occur in Hermitian systems. A recent experiment on organic microcavities with highly polarization-dependent (anisotropic) light-matter coupling (*57*) has demonstrated a diverging quantum metric at the EP, in stark difference to Hermitian systems (*31*).

Unlike previous observations of EPs in optical microcavities (*54*), our demonstration of a non-Hermitian topological invariant relies on hybrid light-matter particles, exciton polaritons, which exhibit strong interactions due to the exciton component (*63*). Therefore, our study offers a new platform for investigating the interplay between the non-Hermitian topology and nonlinearity, which may bring about unexpected phenomena, e.g., similar to self-adaptation in energy transfer (*64*). For example, under a strong circular polarized excitation, the unique strong spin-anisotropic nonlinearity in exciton-polariton systems (*48*, *55*) could potentially lead to an effective real σ_z perturbation with rich tunability. This could provide an efficient pathway for investigating Hermitian and non-Hermitian topological effects in the presence of σ_z perturbations and nonlinearity, even without the need of real magnetic fields.

Last, the strong interactions and very small effective mass of exciton polaritons have successfully enabled the demonstration of collective quantum effects, e.g., bosonic condensation (*65*) and superfluidity (*66*, *67*), at elevated temperatures, in particular, using lead-halide perovskites (*33*, *34*, *68*). Thus, our work paves the way for investigating the interplay between quantum many-body effects and non-Hermitian topology, which is, as yet, an unexplored frontier in non-Hermitian physics (*12*).

MATERIALS AND METHODS

Perovskite microcavity fabrication

Pairs (20.5) of SiO_2 and Ta_2O_5 were deposited on a silicon substrate as the bottom DBR using an electron beam evaporator (OHMIKER-50D). The 142-nm-thick cesium lead bromide perovskite crystal was grown with a vapor phase deposition method on a mica substrate and then transferred onto the bottom DBR by a dry-transfer process with Scotch tape (*33*). Subsequently, a 60-nm-thick poly(methyl methacrylate) protection layer was spin-coated onto the perovskite layer. Another 10.5 pairs of SiO_2 and Ta_2O_5 were deposited onto the structure by the electron beam evaporator, acting as the top DBR to complete the fabrication process.

Optical spectroscopy characterizations

The energy-resolved momentum space PL was mapped by using a home-built angle-resolved PL setup with a motorized translation stage to scan the whole 2D momentum space. In the detection line, a quarter–wave plate, a half–wave plate, and a linear polarizer were used for the detection of polarization-resolved PL mappings in momentum space. A continuous-wave laser (457 nm) with a pump spot of ~10 μm was used to pump the perovskite microcavity, passing through an optical chopper to minimize sample heating. The emission from the perovskite microcavity was collected through a 50× objective (numerical aperture = 0.75, Mitutoyo) and directed to a 550-mm focal length spectrometer (HORIBA iHR550) with a grating of 1200 lines/mm and a liquid nitrogen–cooled charge-coupled device of 256 × 1024 pixels. All measurements were conducted at room temperature.

Non-Hermitian theoretical model

The simple non-Hermitian model in Eqs. 1 and 2 for the exciton-polariton spectrum was derived by simulating the reflectance of a microcavity with an embedded anisotropic cavity spacer and the excitonic transition in the strong coupling regime. We follow the 4 × 4 transfer matrix method in (*46*) but with an addition of the exciton resonance modeled as a Lorentz oscillator.

The transfer matrix calculations and the theoretical model also capture the linewidth behavior of the experiment shown in fig. S4. Regardless of the direction, the linewidth increases with k as the exciton fraction of polariton increases. However, the experimental linewidth increases more or less linearly with k (see fig. S4), compared to the near-parabolic behavior of the numerical simulation. This can arise from the inhomogeneous broadening of the exciton resonance, which is not accounted for in the simulations.

Determination of mode energies and linewidths

To measure the energy and linewidth, we fit Lorentzian functions to the measured spectra at different points in k-space. The energy corresponds to the center, while the linewidth corresponds to the full width at half maximum of the fitted Lorentzian function. Away from the energy crossings, the spectrum displays two peaks and can be fitted with a double Lorentzian function, as shown in fig. S7. Near the energy crossings, there is only one apparent peak since the mode energy separation is smaller than the linewidth. To resolve the individual peaks, we take advantage of the orthogonal pairs (H-V or D-A) of polarized measurements. Each polarized spectrum is fitted with a single Lorentzian as shown in fig. S7, and the orthogonal pair with the largest energy splitting is chosen. This switching between H-V and D-A results in jumps in the extracted energies and linewidths (see Fig. 3, B to F) and small phase jumps in the spectral phase (see Fig. 4, E and F). This is because we are not measuring (or projecting) the eigenstates in their appropriate orthogonal basis. In principle, a full polarization tomography is needed, in addition to the 2D scan of the momentum space, to properly separate the modes and smoothen the jumps in the complex energy and spectral phase. However, this will greatly increase the measurement time and data from 3D to 4D. The current set of data is enough to verify the existence of EPs and measure the half-integer spectral winding in this system.

SUPPLEMENTARY MATERIALS

Supplementary material for this article is available at https://science.org/doi/10.1126/sciadv.abj8905

REFERENCES AND NOTES

1. Y. Tokura, K. Yasuda, A. Tsukazaki, Magnetic topological insulators. *Nat. Rev. Phys.* **1**, 126–143 (2019).
2. A. A. Burkov, Chiral anomaly and transport in Weyl metals. *J. Phys. Condens. Mater.* **27**, 113201 (2015).

3. C. K. Chan, N. H. Lindner, G. Refael, P. A. Lee, Photocurrents in Weyl semimetals. *Phys. Rev. B* **95**, (2017).
4. L. Lu, J. D. Joannopoulos, M. Soljacic, Topological photonics. *Nat. Photonics* **8**, 821–829 (2014).
5. Ş. K. Özdemir, S. Rotter, F. Nori, L. Yang, Parity–time symmetry and exceptional points in photonics. *Nat. Mater.* **18**, 783–798 (2019).
6. R. El-Ganainy, K. G. Makris, M. Khajavikhan, Z. H. Musslimani, S. Rotter, D. N. Christodoulides, Non-Hermitian physics and PT symmetry. *Nat. Phys.* **14**, 11–19 (2018).
7. B. Peng, Ş. K. Özdemir, S. Rotter, H. Yilmaz, M. Liertzer, F. Monifi, C. M. Bender, F. Nori, L. Yang, Loss-induced suppression and revival of lasing. *Science* **346**, 328–332 (2014).
8. W. Chen, Ş. Kaya Özdemir, G. Zhao, J. Wiersig, L. Yang, Exceptional points enhance sensing in an optical microcavity. *Nature* **548**, 192–196 (2017).
9. H. Hodaei, A. U. Hassan, S. Wittek, H. Garcia-Gracia, R. El-Ganainy, D. N. Christodoulides, M. Khajavikhan, Enhanced sensitivity at higher-order exceptional points. *Nature* **548**, 187–191 (2017).
10. C. E. Rüter, K. G. Makris, R. El-Ganainy, D. N. Christodoulides, M. Segev, D. Kip, Observation of parity–time symmetry in optics. *Nat. Phys.* **6**, 192–195 (2010).
11. B. Peng, Ş. K. Özdemir, F. Lei, F. Monifi, M. Gianfreda, G. L. Long, S. Fan, F. Nori, C. M. Bender, L. Yang, Parity–time-symmetric whispering-gallery microcavities. *Nat. Phys.* **10**, 394–398 (2014).
12. E. J. Bergholtz, J. C. Budich, F. K. Kunst, Exceptional topology of non-Hermitian systems. *Rev. Mod. Phys.* **93**, 15005 (2019).
13. A. Ghatak, T. Das, New topological invariants in non-Hermitian systems. *J. Phys. Condens. Matter* **31**, 263001 (2019).
14. S. Yao, Z. Wang, Edge states and topological invariants of non-Hermitian systems. *Phys. Rev. Lett.* **121**, 086803 (2018).
15. Y. Xiong, Why does bulk boundary correspondence fail in some non-Hermitian topological models. *J. Phys. Commun.* **2**, 035043 (2018).
16. F. K. Kunst, E. Edvardsson, J. C. Budich, E. J. Bergholtz, Biorthogonal bulk-boundary correspondence in non-Hermitian systems. *Phys. Rev. Lett.* **121**, 026808 (2018).
17. S. Yao, F. Song, Z. Wang, Non-Hermitian Chern bands. *Phys. Rev. Lett.* **121**, 136802 (2018).
18. T. Liu, Y.-R. Zhang, Q. Ai, Z. Gong, K. Kawabata, M. Ueda, F. Nori, Second-order topological phases in non-hermitian systems. *Phys. Rev. Lett.* **122**, 076801 (2019).
19. C. H. Lee, L. Li, J. Gong, Hybrid higher-order skin-topological modes in nonreciprocal systems. *Phys. Rev. Lett.* **123**, 016805 (2019).
20. M. Brandenbourger, X. Locsin, E. Lerner, C. Coulais, Non-reciprocal robotic metamaterials. *Nat. Commun.* **10**, 4608 (2019).
21. T. Helbig, T. Hofmann, S. Imhof, M. Abdelghany, T. Kiessling, L. W. Molenkamp, C. H. Lee, A. Szameit, M. Greiter, R. Thomale, Generalized bulk–boundary correspondence in non-Hermitian topolectrical circuits. *Nat. Phys.* **16**, 747–750 (2020).
22. L. Xiao, T. Deng, K. Wang, G. Zhu, Z. Wang, W. Yi, P. Xue, Non-Hermitian bulk–boundary correspondence in quantum dynamics. *Nat. Phys.* **16**, 761–766 (2020).
23. D. Leykam, K. Y. Bliokh, C. Huang, Y. D. Chong, F. Nori, Edge modes, degeneracies, and topological numbers in non-Hermitian systems. *Phys. Rev. Lett.* **118**, 040401 (2017).
24. Z. Gong, Y. Ashida, K. Kawabata, K. Takasan, S. Higashikawa, M. Ueda, Topological phases of non-Hermitian systems. *Phys. Rev. X* **8**, 031079 (2018).
25. H. Shen, B. Zhen, L. Fu, Topological band theory for non-Hermitian Hamiltonians. *Phys. Rev. Lett.* **120**, 146402 (2018).
26. M. Atala, M. Aidelsburger, J. T. Barreiro, D. Abanin, T. Kitagawa, E. Demler, I. Bloch, Direct measurement of the Zak phase in topological Bloch bands. *Nat. Phys.* **9**, 795–800 (2013).
27. M. Aidelsburger, M. Lohse, C. Schweizer, M. Atala, J. T. Barreiro, S. Nascimbène, N. R. Cooper, I. Bloch, N. Goldman, Measuring the Chern number of Hofstadter bands with ultracold bosonic atoms. *Nat. Phys.* **11**, 162–166 (2015).
28. W. Hu, J. C. Pillay, K. Wu, M. Pasek, P. P. Shum, Y. D. Chong, Measurement of a topological edge invariant in a microwave network. *Phys. Rev. X* **5**, 011012 (2015).
29. S. Mittal, S. Ganeshan, J. Fan, A. Vaezi, M. Hafezi, Measurement of topological invariants in a 2D photonic system. *Nat. Photonics* **10**, 180–183 (2016).
30. H. Zhou, C. Peng, Y. Yoon, C. W. Hsu, K. A. Nelson, L. Fu, J. D. Joannopoulos, M. Soljačić, B. Zhen, Observation of bulk Fermi arc and polarization half charge from paired exceptional points. *Science* **359**, 1009–1012 (2018).
31. A. Ghatak, M. Brandenbourger, J. van Wezel, C. Coulais, Observation of non-Hermitian topology and its bulk-edge correspondence in an active mechanical metamaterial. *Proc. Natl. Acad. Sci. U.S.A.* **117**, 29561–29568 (2020).
32. C. Schneider, K. Winkler, M. D. Fraser, M. Kamp, Y. Yamamoto, E. A. Ostrovskaya, S. Höfling, Exciton-polariton trapping and potential landscape engineering. *Rep. Prog. Phys.* **80**, 016503 (2016).
33. R. Su, S. Ghosh, J. Wang, S. Liu, C. Diederichs, T. C. H. Liew, Q. Xiong, Observation of exciton polariton condensation in a perovskite lattice at room temperature. *Nat. Phys.* **16**, 301–306 (2020).
34. M. Dusel, S. Betzold, O. A. Egorov, S. Klembt, J. Ohmer, U. Fischer, S. Höfling, C. Schneider, Room temperature organic exciton–polariton condensate in a lattice. *Nat. Commun.* **11**, 2863 (2020).
35. S. Klembt, T. H. Harder, O. A. Egorov, K. Winkler, R. Ge, M. A. Bandres, M. Emmerling, L. Worschech, T. C. H. Liew, M. Segev, C. Schneider, S. Höfling, Exciton-polariton topological insulator. *Nature* **562**, 552–556 (2018).
36. A. Gianfrate, O. Bleu, L. Dominici, V. Ardizzone, M. De Giorgi, D. Ballarini, G. Lerario, K. W. West, L. N. Pfeiffer, D. D. Solnyshkov, D. Sanvitto, G. Malpuech, Measurement of the quantum geometric tensor and of the anomalous Hall drift. *Nature* **578**, 381–385 (2020).
37. L. Polimeno, M. De Giorgi, G. Lerario, L. De Marco, L. Dominici, V. Ardizzone, M. Pugliese, C. T. Prontera, V. Maiorano, A. Moliterni, C. Giannini, V. Olieric, G. Gigli, D. Ballarini, D. Solnyshkov, G. Malpuech, D. Sanvitto, Tuning the Berry curvature in 2D perovskite. arXiv:2007.14945 (2020).
38. J. Ren, Q. Liao, F. Li, Y. Li, O. Bleu, G. Malpuech, J. Yao, H. Fu, D. Solnyshkov, Nontrivial band geometry in an optically active system. *Nat. Commun.* **12**, 689 (2021).
39. W. D. Heiss, Exceptional points of non-Hermitian operators. *J. Phys. A Math. Gen.* **37**, 2455–2464 (2004).
40. T. Gao, E. Estrecho, K. Y. Bliokh, T. C. H. Liew, M. D. Fraser, S. Brodbeck, M. Kamp, C. Schneider, S. Höfling, Y. Yamamoto, F. Nori, Y. S. Kivshar, A. G. Truscott, R. G. Dall, E. A. Ostrovskaya, Observation of non-Hermitian degeneracies in a chaotic exciton-polariton billiard. *Nature* **526**, 554–558 (2015).
41. T. Gao, G. Li, E. Estrecho, T. C. H. Liew, D. Comber-Todd, A. Nalitov, M. Steger, K. West, L. Pfeiffer, D. W. Snoke, A. V. Kavokin, A. G. Truscott, E. A. Ostrovskaya, Chiral modes at exceptional points in exciton-polariton quantum fluids. *Phys. Rev. Lett.* **120**, 065301 (2018).
42. P. Comaron, V. Shahnazaryan, W. Brzezicki, T. Hyart, M. Matuszewski, Non-Hermitian topological end-mode lasing in polariton systems. *Phys. Rev. Res.* **2**, 022051 (2020).
43. S. Mandal, R. Banerjee, E. A. Ostrovskaya, T. C. H. Liew, Nonreciprocal transport of exciton polaritons in a non-Hermitian chain. *Phys. Rev. Lett.* **125**, 123902 (2020).
44. L. Pickup, H. Sigurdsson, J. Ruostekoski, P. G. Lagoudakis, Synthetic band-structure engineering in polariton crystals with non-Hermitian topological phases. *Nat. Commun.* **11**, 4431 (2020).
45. C. Leyder, M. Romanelli, J. P. Karr, E. Giacobino, T. C. H. Liew, M. M. Glazov, A. V. Kavokin, G. Malpuech, A. Bramati, Observation of the optical spin Hall effect. *Nat. Phys.* **3**, 628–631 (2007).
46. S. Richter, T. Michalsky, C. Sturm, B. Rosenow, M. Grundmann, R. Schmidt-Grund, Exceptional points in anisotropic planar microcavities. *Phys. Rev. A* **95**, 023836 (2017).
47. G. Panzarini, L. C. Andreani, A. Armitage, D. Baxter, M. S. Skolnick, V. N. Astratov, J. S. Roberts, A. V. Kavokin, M. R. Vladimirova, M. A. Kaliteevski, Cavity-polariton dispersion and polarization splitting in single and coupled semiconductor microcavities. *Phys. Solid State* **41**, 1223–1238 (1999).
48. H. Terças, H. Flayac, D. D. Solnyshkov, G. Malpuech, Non-Abelian gauge fields in photonic cavities and photonic superfluids. *Phys. Rev. Lett.* **112**, 066402 (2014).
49. A. Fieramosca, L. Polimeno, G. Lerario, L. De Marco, M. De Giorgi, D. Ballarini, L. Dominici, V. Ardizzone, M. Pugliese, V. Maiorano, G. Gigli, C. Leblanc, G. Malpuech, D. Solnyshkov, D. Sanvitto, Chromodynamics of photons in an artificial non-Abelian magnetic Yang-Mills field. arXiv:1912.09684 (2019).
50. R. Su, S. Ghosh, T. C. H. Liew, Q. Xiong, Optical switching of topological phase in a perovskite polariton lattice. *Sci. Adv.* **7**, eabf8049 (2021).
51. M. V. Berry, M. R. Dennis, The optical singularities of birefringent dichroic chiral crystals. *Proc. R. Soc. Lond. Ser. A* **459**, 1261–1292 (2003).
52. M. A. Becker, R. Vaxenburg, G. Nedelcu, P. C. Sercel, A. Shabaev, M. J. Mehl, J. G. Michopoulos, S. G. Lambrakos, N. Bernstein, J. L. Lyons, T. Stöferle, R. F. Mahrt, M. V. Kovalenko, D. J. Norris, G. Rainò, A. L. Efros, Bright triplet excitons in caesium lead halide perovskites. *Nature* **553**, 189–193 (2018).
53. R. Su, C. Diederichs, J. Wang, T. C. H. Liew, J. Zhao, S. Liu, W. Xu, Z. Chen, Q. Xiong, Room-temperature polariton lasing in all-inorganic perovskite nanoplatelets. *Nano Lett.* **17**, 3982–3988 (2017).
54. S. Richter, H.-G. Zirnstein, J. Zúñiga-Pérez, E. Krüger, C. Deparis, L. Trefflich, C. Sturm, B. Rosenow, M. Grundmann, R. Schmidt-Grund, Voigt exceptional points in an anisotropic ZnO-based planar microcavity: Square-root topology, polarization vortices, and circularity. *Phys. Rev. Lett.* **123**, 227401 (2019).
55. D. Biegańska, M. Pieczarka, E. Estrecho, M. Steger, D. W. Snoke, K. West, L. N. Pfeiffer, M. Syperek, A. G. Truscott, E. A. Ostrovskaya, Collective excitations of exciton-polariton condensates in a synthetic gauge field. arXiv:2011.13290 (2020).
56. W. Gao, X. Li, M. Bamba, J. Kono, Continuous transition between weak and ultrastrong coupling through exceptional points in carbon nanotube microcavity exciton–polaritons. *Nat. Photonics* **12**, 362–367 (2018).
57. Q. Liao, C. Leblanc, J. Ren, F. Li, Y. Li, D. Solnyshkov, G. Malpuech, J. Yao, H. Fu, Experimental measurement of the divergent quantum metric of an exceptional point. *Phys. Rev. Lett.* **127**, 107402 (2020).

58. A. Cerjan, S. Fan, Achieving arbitrary control over pairs of polarization states using complex birefringent metamaterials. *Phys. Rev. Lett.* **118**, 253902 (2017).
59. P. C. Sercel, Z. V. Vardeny, A. L. Efros, Circular dichroism in non-chiral metal halide perovskites. *Nanoscale* **12**, 18067–18078 (2020).
60. J. Li, J. Li, R. Liu, Y. Tu, Y. Li, J. Cheng, T. He, X. Zhu, Autonomous discovery of optically active chiral inorganic perovskite nanocrystals through an intelligent cloud lab. *Nat. Commun.* **11**, 2046 (2020).
61. D. D. Solnyshkov, C. Leblanc, L. Bessonart, A. Nalitov, J. Ren, Q. Liao, F. Li, G. Malpuech, Quantum metric and wave packets at exceptional points in non-Hermitian systems. *Phys. Rev. B* **103**, 125302 (2021).
62. T. Hofmann, T. Helbig, F. Schindler, N. Salgo, M. Brzezińska, M. Greiter, T. Kiessling, D. Wolf, A. Vollhardt, A. Kabaši, C. H. Lee, A. Bilušić, R. Thomale, T. Neupert, Reciprocal skin effect and its realization in a topolectrical circuit. *Phys. Rev. Res.* **2**, 023265 (2020).
63. J. Wu, S. Ghosh, R. Su, A. Fieramosca, T. C. H. Liew, Q. Xiong, Nonlinear parametric scattering of exciton polaritons in perovskite microcavities. *Nano Lett.* **21**, 3120–3126 (2021).
64. S. Assawaworrarit, X. Yu, S. Fan, Robust wireless power transfer using a nonlinear parity–time-symmetric circuit. *Nature* **546**, 387–390 (2017).
65. J. Kasprzak, M. Richard, S. Kundermann, A. Baas, P. Jeambrun, J. M. J. Keeling, F. M. Marchetti, M. H. Szymańska, R. André, J. L. Staehli, V. Savona, P. B. Littlewood, B. Deveaud, L. S. Dang, Bose–Einstein condensation of exciton polaritons. *Nature* **443**, 409–414 (2006).
66. A. Amo, J. Lefrère, S. Pigeon, C. Adrados, C. Ciuti, I. Carusotto, R. Houdré, E. Giacobino, A. Bramati, Superfluidity of polaritons in semiconductor microcavities. *Nat. Phys.* **5**, 805–810 (2009).
67. G. Lerario, A. Fieramosca, F. Barachati, D. Ballarini, K. S. Daskalakis, L. Dominici, M. De Giorgi, S. A. Maier, G. Gigli, S. Kéna-Cohen, D. Sanvitto, Room-temperature superfluidity in a polariton condensate. *Nat. Phys.* **13**, 837–841 (2017).
68. R. Su, J. Wang, J. Zhao, J. Xing, W. Zhao, C. Diederichs, T. C. H. Liew, Q. Xiong, Room temperature long-range coherent exciton polariton condensate flow in lead halide perovskites. *Sci. Adv.* **4**, eaau0244 (2018).

Acknowledgments

Funding: Q.X. acknowledges the National Natural Science Foundation of China (no. 12020101003), strong support from the State Key Laboratory of Low-Dimensional Quantum Physics, and start-up grant from Tsinghua University. T.C.H.L. acknowledges the support from Singapore Ministry of Education via AcRF Tier 3 Programme "Geometrical Quantum Materials" (MOE2018-T3-1-002) and AcRF Tier 2 grants (MOE2017-T2-1-001, MOE2018-T2-02-068, and MOE2019-T2-1-004). E.E., E.A.O., M.W., and M.P. acknowledge support from the Australian Research Council (ARC) through the Centre of Excellence Grant CE170100039. M.P. also acknowledges support from the Foundation for Polish Science in the START programme.

Author contributions: Q.X. and E.A.O. supervised and guided this research. R.S. and Y.H. designed the setup. R.S. fabricated the sample. R.S. and E.E. designed and performed the experiments. E.E., R.S., and D.B. analyzed and interpreted the data with input from M.W., M.P., A.G.T., T.C.H.L., E.A.O., and Q.X. E.E. developed the theoretical model and performed the theoretical calculations. E.E., R.S., and E.A.O. wrote the manuscript with input from all authors.
Competing interests: The authors declare that they have no competing interests. **Data and materials availability:** All data needed to evaluate the conclusions in the paper are present in the paper and/or the Supplementary Materials.

Submitted 9 June 2021
Accepted 13 September 2021
Published 3 November 2021
10.1126/sciadv.abj8905

ScienceAdvances

Direct measurement of a non-Hermitian topological invariant in a hybrid light-matter system

Rui SuEliezer EstrechoD#bówka Biega#skaYuqing HuangMatthias WurdackMaciej PieczarkaAndrew G. TruscottTimothy C. H. LiewElena A. OstrovskayaQihua Xiong

Sci. Adv., 7 (45), eabj8905. • DOI: 10.1126/sciadv.abj8905

Science Advances (ISSN) is published by the American Association for the Advancement of Science. 1200 New York Avenue NW, Washington, DC 20005. The title *Science Advances* is a registered trademark of AAAS.